Journal of Materials Chemistry A

PAPER

View Article Online
View Journal | View Issue

Cite this: J. Mater. Chem. A, 2015, 3, 3794

Superiority of the bi-phasic mixture of a tin-based alloy nanocomposite as the anode for lithium ion batteries†

Xue Li,[a] Xinyi He,[a] Yuefeng Xu,[a] Ling Huang,*[a] Juntao Li,[b] Shigang Sun[a] and Jinbao Zhao[a]

Received 13th December 2014
Accepted 24th December 2014

DOI: 10.1039/c4ta06862a

www.rsc.org/MaterialsA

The nanostructured mixture of a Sn_2Fe and Sn_2Co alloy composite with uniform cubic shaped particles has been synthesized by a reduction-thermal diffusion alloying reaction. The textural properties of the as-prepared samples were characterized by field-emission scanning electron microscopy, transmission electron microscopy and powder X-ray diffraction. Compared with the Sn_2Fe alloy, the alloy composite exhibits better reversibility and cycle performance. At a charge/discharge current density of 50 mA g^{-1}, a reversible capacity of 510 mA h g^{-1} can be maintained after 50 cycles, and its capacity in the 50th cycle was retained at *ca.* 85% of that in the second cycle. When the current density is increased to 1000 mA g^{-1}, a reversible capacity of 443 mA h g^{-1} can be still obtained. The *ab initio* simulation results indicate that Sn_2Fe and Sn_2Co have similar crystal structures, demonstrating that the two kinds of alloys can be mixed uniformly by the thermal diffusion alloying reaction. The superior electrochemical performance can be attributed to the homogeneously dispersed inactive metallic material (Fe and Co) nanostructure, which partly accommodates the volume change and also retains the integrity of the active material and matrix, resulting in good cycle performance of the composite electrode.

Introduction

Lithium-ion batteries as the most suitable power of portable electronic devices provide a lot of convenience to people. Because of the high performance of mobile electronic devices, people have higher expectations of using lithium-ion batteries with energy density. Due to the small room for the development of high capacity cathode materials, the capacity increase for LIBs in the past five years is almost similar to the improved performance of anode materials. Therefore, much attention has been focused on new type of anode materials with novel structures prepared by original and facile methods.[1–5] At present, graphite is normally used as an anode material for lithium ion batteries with a relatively low theoretical capacity of 372 mA h g^{-1}. Compared with graphite, tin-based materials have been regarded as the one of the candidates with the greatest potential because of their high theoretical specific capacity (994 mA h g^{-1}).[6,7] However, it is well known that pure tin metal electrodes suffer from large volume expansion (about 358%)[8] during the charge–discharge process, leading to mechanical disintegration and a very poor cycle life. To solve this problem, Winter *et al.* have proposed that preparing alloys or composite materials can improve the cycling performance.[9] For the alloy materials, the Li_xMSn phase or mixture phase of $Li_{4.4}Sn$ and metal M can be formed during the alloying–dealloying process. Among these phases, the inactive phase M offers a buffer matrix to relieve volume expansion during the charge–discharge process; moreover, it plays a role in maintaining the integrity between the particles, the active material and the current collector.[10] These alloys such as Cu_6Sn_5,[11] SnNi,[12] SnSb,[13] SnCoC,[14] and SnSbM,[15] have shown good reversible specific capacities. Among tin-based alloys, SnFe alloy has received much attention in recent years with its advantage of good conductivity, low cost, open architecture and high capacity.[16] Zhang *et al.* demonstrated that the Sn_2Fe alloy with particle size of 80 nm derived from hydrothermal synthesis could deliver reversible capacity of 500 mA h g^{-1}.[17,18] Chamas *et al.* studied the electrochemical performance of nanoscale Sn_2Fe particles and found the nanoscale material exhibited relatively high capacity but there was a rapid decay after 40 cycles.[19]

Thus, higher capacity can be obtained for SnFe alloy at the nanoscale; however, the cycling performance of the nanomaterial is still poor, and there is always rapid capacity fading after 30 cycles. In this work, the cubic bi-phase SnFeCo alloy was fabricated by a chemical reduction-thermal diffusion alloying reaction, with the particle size of 106 nm in narrow distribution.

[a]Department of Chemistry, College of Chemistry and Chemical Engineering, State Key Laboratory of Physical Chemistry of Solid Surfaces, Xiamen University, Xiamen, 361005, China. E-mail: huangl@xmu.edu.cn

[b]College of Energy Research, Xiamen University, Xiamen, 361005, China

† Electronic supplementary information (ESI) available: Fig. S1 (a) TEM image of one single SnFeCo alloy particle (b) the corresponding HR-TEM image from the selected area. See DOI: 10.1039/c4ta06862a

As anode material for lithium ion batteries, the alloy composite exhibits better reversibility and cycle performance. Based on density functional theory (DFT), we have used the Vienna *Ab initio* Simulation Package (VASP) to calculate crystal structure parameters of the as-prepared alloy material and explore the electrochemical process of the as-prepared Sn-based composite material. The post-cycling microstructure characterization and XPS spectrum analysis are also carried out to investigate the alloy electrodes. All the data consistently prove that the bi-phase mixture of the tin-based alloy is superior for lithium storage compared with the single-phase alloy.

Experimental section

Material preparation

In a typical synthesis of intermetallic SnFeCo nanocrystals, 1.0 g of PVP was dissolved in 50 ml tetraethylene glycol (TEG) at room temperature. The solution was heated to 170 °C, and then $SnCl_2$ (1.3 g in 10 ml of TEG) was added. A freshly prepared solution of $NaBH_4$ (2.64 g in 50 ml of TEG) was then added dropwise with stirring. After 10 min at 170 °C, iron (0.74 g $FeCl_3 \cdot 6H_2O$ in 30 ml of TEG) and cobalt ion (0.5 g $CoCl_2 \cdot 6H_2O$ in 30 ml of TEG) solutions were sequentially added. The solution was then heated to 190 °C with continued stirring. After alloying for 2 h, a color change from gray to black was observed. The preparation was carried out under argon to avoid the oxidation of the ions. The resulting powders were separated from the solvent by centrifugation, washed with ethanol and dried under vacuum at 80 °C. The same approach was used for Sn_2Fe, except for the cobalt ions solution.

Material characterization

The morphologies and structures of the as-prepared intermetallic SnFeCo nanoparticles were characterized by field emission scanning electron microscopy (LEO 1530, HITACHI S-4800) and high resolution transmission electron microscopy (HRTEM, JEM-2100). Powder X-ray diffraction (XRD, Philips X'pert Pro Super X-ray diffract meter, Cu Kα radiation) was used for phase analysis. Inductively Coupled Plasma Atomic Emission Spectrometry (ICP-AES, BIRAD PS-4, 1.1 kw, 27 MHz) was used for the exact element content analysis. The X-ray photoelectron spectroscopy (XPS) analysis was performed with a QUANTUM 2000 spectrometer using focused monochromatized Al Kα radiation (1486.6 eV). The pass energy was 60 eV for the survey spectra and 20 eV for some elements.

Electrochemical measurements

The electrochemical performance of as-prepared intermetallic SnFeCo nanocrystals was characterized by assembling them into coin cells (type CR2025) in an argon-filled glove box under conditions where the moisture and oxygen content were both below 1 ppm. The anode was prepared by spreading a mixture of 80 wt% intermetallic SnFeCo powder, 10 wt% acetylene black and 10 wt% LA133 binder onto a copper foil current collector. The as-prepared electrodes were dried at 80 °C in a vacuum oven for 12 h. The anode was separated from lithium by a separator (Celgard 2400). The electrolyte was made from $LiPF_6$ (1 M) in a mixture of ethylene carbonate (EC)/dimethyl carbonate (DMC)/diethyl carbonate (DEC) in a volume ratio of 1 : 1 : 1 with 2 wt% vinylene carbonate (VC) as an additive. The cells were galvanostatically charged and discharged in a battery test system (LAND-V34, Land Electronic Co., Ltd., Wuhan) at a current density of 50 mA g^{-1} for a cut-off voltage of 0.02–1.5 V (*vs.* Li/Li^+) at room temperature.

Calculation procedure

All the calculations reported herein were performed based on density functional theory (DFT) as implemented in the Vienna *Ab initio* Simulation Package (VASP).[20,21] The electronic exchange correlation energy was modeled using the Perdew–Burke–Ernzerhof (PBE) function within the generalized gradient approximation (GGA).[22] The wave functions were expanded in plane-wave basis up to a kinetic energy cut-off of 350 eV. Brillouin zone integrations were performed by using special *k*-point sampling of the Monkhorst–Pack scheme[23] with a 5 × 5 × 6 grid. The atomic positions and cell parameters are fully relaxed until the Hellmann–Feynman forces on all the atoms were smaller than 0.01 eV $Å^{-1}$.

Results and discussion

Fig. 1 shows the XRD pattern of the SnFeCo alloy. The pure Sn_2Fe phase (JCPDS no: 00-004-0745) can be found in the XRD pattern, whose peaks at 33.63°, 35.01°, 38.99°, 43.81°, 56.35°, 61.06°, 67.21° and 70.61° correspond to the diffraction peaks of (002), (211), (122), (202), (002), (213), (402) and (004) crystal facets. There are no peaks of SnCo alloy and impurities in this pattern, which may be due to the low quantity of cobalt. All the peaks are very sharp, indicating the alloy structure is crystallized.

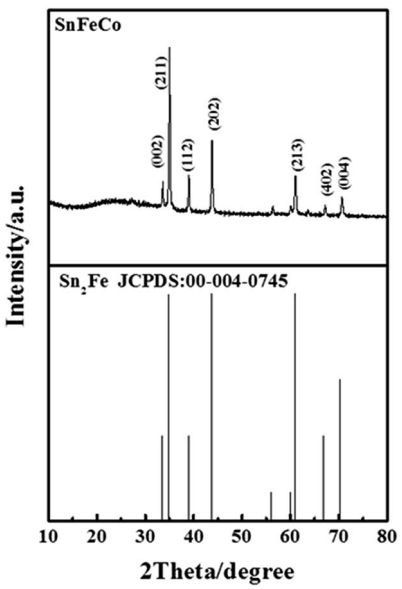

Fig. 1 XRD pattern of the SnFeCo alloy composite.

In order to further verify the composition of the material, ICP-AES analysis was carried out and the results are listed in Table 1. As shown in the table, the output ratio is lower than the input ratio for cobalt. This is probably because of the excessive cobalt loss in the centrifugal cleaning process and the formation of the SnCo alloy with tin. In accordance with the elemental ratio, the theoretical capacity was calculated as 781 mA h g^{-1}.

The textural properties were characterized by scanning electron microscopy (SEM), as shown in Fig. 2(a). From Fig. 2, we can see the SnFeCo alloy particles are in a cubic-like morphology because of the body-centered tetragonal structure. The distribution of the grain-size of the particles is presented in Fig. 2(b), and the average particle size is about 106 nm with narrow distribution.

The dark-field diffraction in Fig. 3(a) shows that one big particle is composed of various surfaces with different brightness levels. The corresponding SAED patterns of Fig. 3(a) marked with"1"and"2"are presented in Fig. 3(b) and (c), respectively. The SAED pattern in Fig. 3(b) shows a single crystal structure that can be indexed to the (211) plane of Sn_2Fe (2.58 Å), consistent with the XRD results. However, the SAED pattern in Fig. 3(c) can be indexed to two kinds of single crystal planes. The spots marked with "△" could be indexed to the (211) plane of Sn_2Fe (2.58 Å, JCPDS: 00-004-0745), and the spots marked with "○" could be indexed to the (211) plane of Sn_2Co (2.51 Å, JCPDS: 03-065-5843).

The TEM images in Fig. 4 are further evidence that the as-prepared alloy is a biphasic mixture. From the HR-TEM image (Fig. 4(b)), we can see that there are two crystal planes combined together with an angle of 49.1°. The two lattice fringes with the lattice spacing of 2.71 Å and 2.58 Å, match fairly well with the (002) plane for Sn_2Co and the (211) plane for Sn_2Fe.

To identify the assignment of the elements in the alloy mixture, EDX spectra were obtained from the corresponding areas in Fig. 5(a) and the atomic ratios are displayed in Table 2. The TEM image in Fig. 5(a) reveals that one big particle is always formed from some small grains with obvious grain boundaries. The element distribution in Table 2 indicates that the low quantity of cobalt is evenly distributed.

In consideration of the data above, we can confirm that the composite material is composed of two kinds of alloy: Sn_2Fe and Sn_2Co. Based on the existing data we can make the following speculation: all the Co formed the Sn_2Co alloy with Sn (as Sn_2Co has lower Gibbs Energy and better chemical stability than Sn_2Fe, which is shown in Table 3 in the following section) and a small amount of Fe formed iron oxides due to the higher oxidation activity compared with Sn and Co (some lattice fringes attributed to Fe_2O_3 are found in HR-TEM diffraction patterns Fig. S1†). According to the speculation, we can calculate the ratio of these two alloys: $Sn_2Fe : Sn_2Co = 0.86 : 0.14$.

Table 1 The mol ratio of elements of SnFeCo alloy composites

Element	Input ratio	Output ratio
Fe	1.00	1.00
Co	0.20	0.14
Sn	2.00	2.00

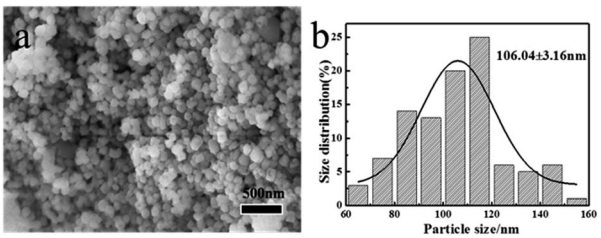

Fig. 2 (a) SEM image of the SnFeCo alloy composite (b) distribution of the grain-size of the SnFeCo alloy composite.

To make the whole reaction process more clear and straightforward, we have proposed a possible growth mechanism of the SnFeCo alloy composite based on the above discussion (as shown in Fig. 6). First, Sn^{2+} was reduced to Sn by $NaBH_4$ coated with PVP. In the second step, Fe^{3+} and Co^{2+} were adsorbed to the surface of the Sn particles through the PVP molecules and were reduced to Fe and Co under the effect of $NaBH_4$. Finally, the inter-diffusion process of these metals occurred at a relatively high temperature, which formed Sn_2Fe and Sn_2Co with the ratio of $Sn_2Fe : Sn_2Co = 0.86 : 0.14$.

Fig. 7(a) presents the data in terms of the cycling performance of the SnFeCo alloy composite electrode and Sn_2Fe alloy electrode at a current density of 50 mA h g^{-1}. The first discharge capacity is 828 mA h g^{-1} and the initial coulombic efficiency is 71%. After 50 cycles, the reversible discharge capacity slightly decreases from 585 mA h g^{-1} to 507 mA h g^{-1} with high retention of 87% of that in the second cycle. Compared with the SnFeCo alloy, the Sn_2Fe alloy electrode has shown a poorer cycling performance. The first discharge capacity is 799 mA h g^{-1} and the initial coulombic efficiency was 68%. After 30 cycles, the reversible discharge capacity rapidly decreases

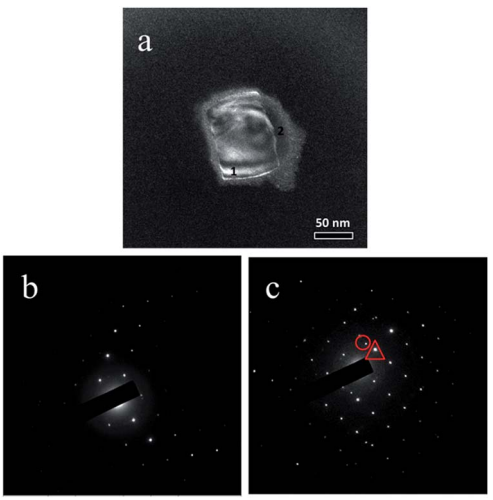

Fig. 3 TEM images of SnFeCo alloy composite (a) dark-field diffraction of SnFeCo alloy composite (b) the corresponding SAED patterns of SnFeCo alloy composite from the selected area marked with "△"(c) the corresponding SAED patterns of SnFeCo alloy composite from the selected area marked with "○".

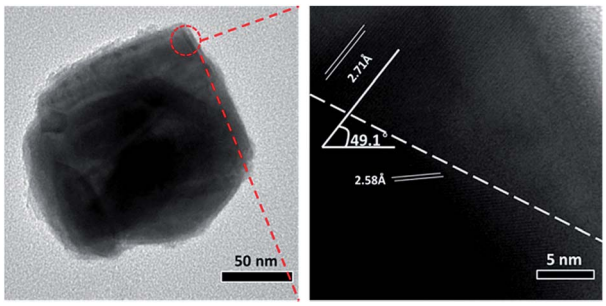

Fig. 4 (a) TEM image of one single SnFeCo alloy particle, and (b) the corresponding HR-TEM image from the selected area.

from 541 mA h g^{-1} to 0 mA h g^{-1}. The rate capacity of the SnCoFe composite electrode is demonstrated in Fig. 7(b), which illustrates a stable cyclic response at progressively increasing rates. Even with the current density of 1000 mA h g^{-1}, the electrode can still deliver about 443 mA h g^{-1}, demonstrating that the biphasic mixture composite exhibits good electrochemical performance.

The SnFeCo alloy composite electrode charge/discharge performance of 1st, 2nd, 10th and 50th cycles is illustrated in Fig. 8(a). The extra discharge capacity in the first cycle may be attributed to the side reaction on the nanomaterial surface. The first discharge capacity fade may be caused by the irreversible lithium loss due to the formation of a solid electrolyte (SEI) layer.[24] The first discharge step produced a long slope voltage plateau at 1.5–0.02 V, which is associated with the intercalation of oxides or the decomposition of electrolyte. The voltage plateau at around 0.5 V, exhibiting a typical trend for tin-based electrodes, is attributed to the alloying reaction as follows:[25]

$$Sn_2Fe + 8.8Li^+ + 8.8e^- \rightarrow 2Li_{4.4}Sn + Fe \quad (1)$$

$$Li_{4.4}Sn \leftrightarrow Sn + 4.4\ Li^+ + 4.4e^- \quad (2)$$

$$Sn_2Co + 8.8Li^+ + 8.8e^- \rightarrow 2Li_{4.4}Sn + Co \quad (3)$$

$$Li_{4.4}Sn \leftrightarrow Sn + 4.4\ Li^+ + 4.4e^- \quad (4)$$

To understand the electrochemical behaviours in the 1st, 2nd, 10th and 50th cycles, differential capacity curves were recorded and are compared in Fig. 8(b). In the first cycle, there are three irreversible reduction peaks at 0.11 V, 0.71 V and 1.07 V. The first peak is generally attributed to the abovementioned irreversible reaction (1) (ref. 26) and disappears in the subsequent cycles, which indicates that the reversible reaction (2) will become the dominant reaction after the initial cycle.[27] The other peaks may correspond to the reduction of tin oxides or the formation of a solid electrolyte interphase (SEI) layer.[28,29] In the subsequent cycles, reduction peaks around 0.3 V and 0.56 V are attributed to the formation of the Li–Sn alloy.[30–32] The peak weakens after the 50th cycle, which indicates the decline in volume expansion.[19,33] During the discharge process, three peaks around 0.45 V, 0.59 V and 0.75 V correspond to the de-

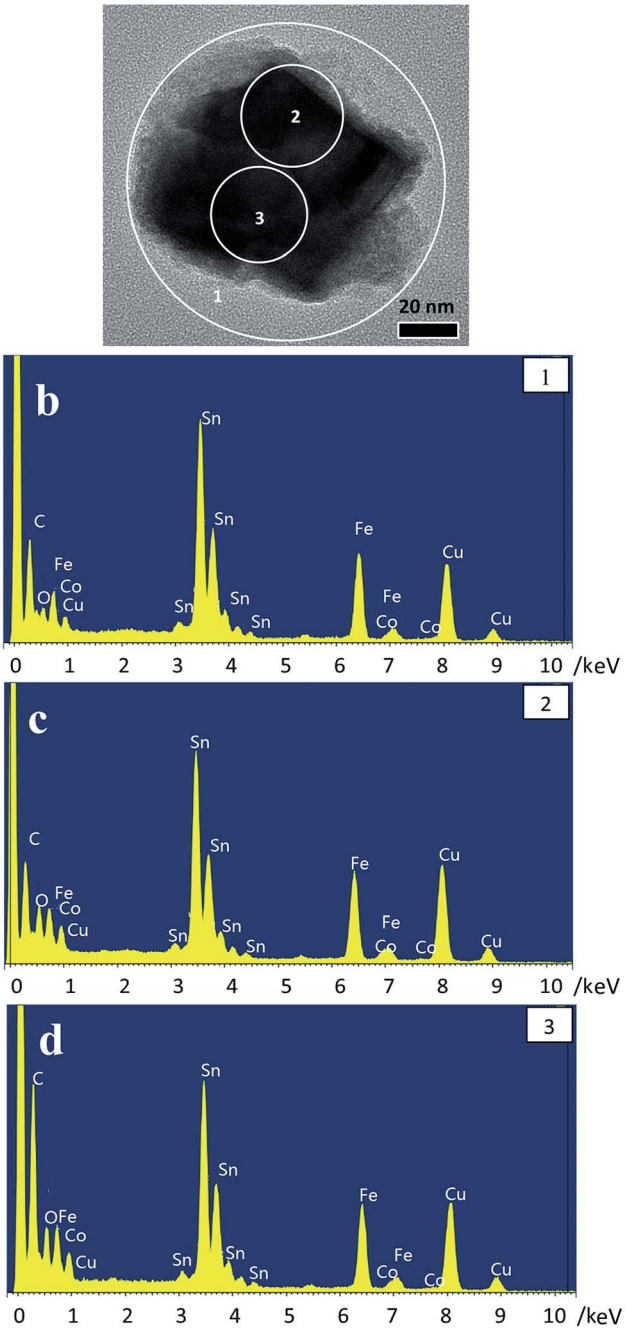

Fig. 5 (a) TEM image of one single SnFeCo alloy particle (b) the corresponding EDX image from the selected area 1 in (a), (c) the corresponding EDX image from the selected area 2 in (a), (d) the corresponding EDX image from the selected area 3 in (a).

Table 2 The distribution of the element in Fig. 5

Element	Area 1	Area 2	Area 3
Fe	16.46%	17.41%	12.40%
Co	1.38%	0.86%	0.97%
Sn	24.46%	27.68%	19.63%

Table 3 The crystal structure simulation results of Sn_2Fe, Sn_2Co, Fe and Co through the VASP method

	Lattice parameter Å	Space group	Cell volume Å^3	Gibbs energy kJ mol^{-1}
Sn_2Fe	$a = b = 6.38$ $c = 5.46$	$I4/mcm$ (tetragonal)	222.41	1.516×10^3
Sn_2Co	$a = b = 6.37$ $c = 5.46$	$I4/mcm$ (tetragonal)	221.88	1.444×10^3
Fe	$a = b = c = 2.75$	$Im\bar{3}m$ (fcc)	20.90	0.757×10^3
Co	$a = b = c = 3.45$	$Fm3m$ (fcc)	41.23	0.425×10^3

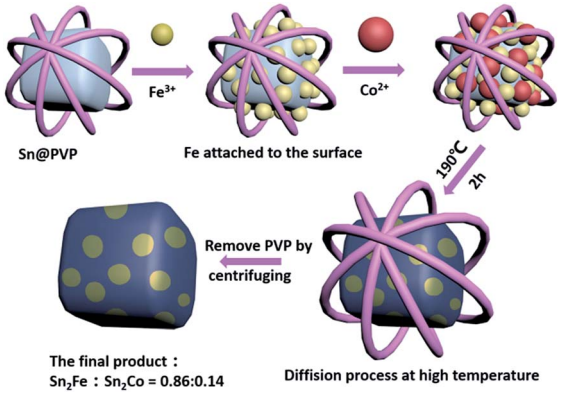

Fig. 6 Schematic illustration of the formation mechanism of SnFeCo alloy composites.

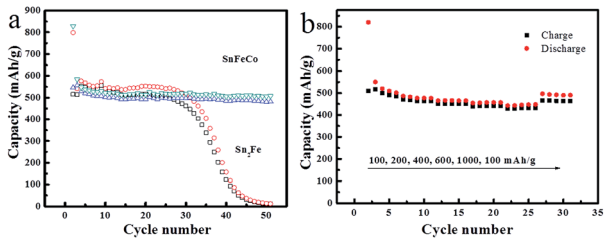

Fig. 7 (a) Cycle performances of the SnFeCo alloy composite and Sn_2Fe alloy electrodes (b) rate performance of the SnFeCo alloy composite.

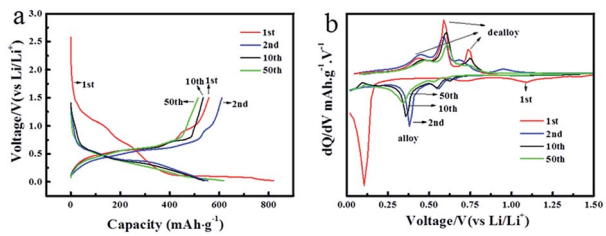

Fig. 8 (a) Charge/discharge curves of the SnFeCo alloy composite electrode (b) differential capacity curves of the SnFeCo alloy electrode.

alloying process of Li_xSn.[28] The dealloying peak around 0.75 V represents the agglomeration of Sn atoms.[34] In this work, we prepared tin-based alloys to avoid this process. As a result, there is a weak peak around 0.75 V with decay in subsequent cycles, which indicates that the electrode material has a good cycling performance without obvious agglomeration.

In consideration of the relationship between the crystal structure change and the mechanism of the electrochemical reaction, we have used the Vienna *Ab initio* Simulation Package (VASP) to calculate the crystal structure parameters of the as-prepared alloy. The simulation results are shown in Table 3, and the schematic diagram of the mechanism of the electrochemical reaction is displayed in Fig. 9 (where the gray balls represent tin, the blue balls represent copper, the yellow balls represent iron and the green balls represent lithium). It should be noted that Sn_2Fe and Sn_2Co have similar crystal structures: (1) the space groups are both tetragonal, (2) they have similar lattice parameters (Sn_2Fe: $a = b = 6.38$ Å $c = 5.46$ Å, Sn_2Co: $a = b = 6.37$ Å $c = 5.46$ Å), and (3) they have similar cell volume (Sn_2Fe: 222.41 Å^3, Sn_2Co: 221.88 Å^3). These results can be another proof that the two kinds of alloys can be mixed uniformly by the facile thermal diffusion alloying reaction.

Considering the abovementioned data, the mechanism of the electrochemical reaction of the alloy composite can be summarized as shown in Fig. 9. In the discharging process, the composite is alloyed to form $Li_{4.4}Sn$ and relevant metallic material, and the volume expands several times. It dealloys to tin with a shrink in volume after the charging process. The inactive phase M (M = Fe, Co) offers a buffer matrix to relieve the volume expansion during the charge–discharge process and also plays a role in maintaining the integrity between the particles, the active material and the current collector.

In order to illuminate the superiority of the bi-phasic mixture of the tin-based alloy further, we analyzed the post-cycling microstructure characterization. As shown in Fig. 10, we can see the particle reunion tends to occur easily in a single-phase (due to the soft texture and active surfaces of $Li_{4.4}Sn$ and

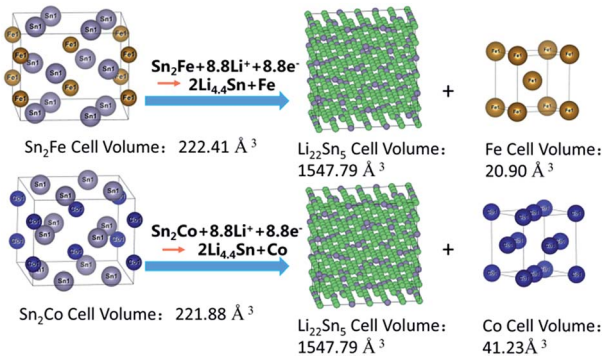

Fig. 9 Schematic of the electrochemical mechanism of the Sn_2Fe and Sn_2Co composite.

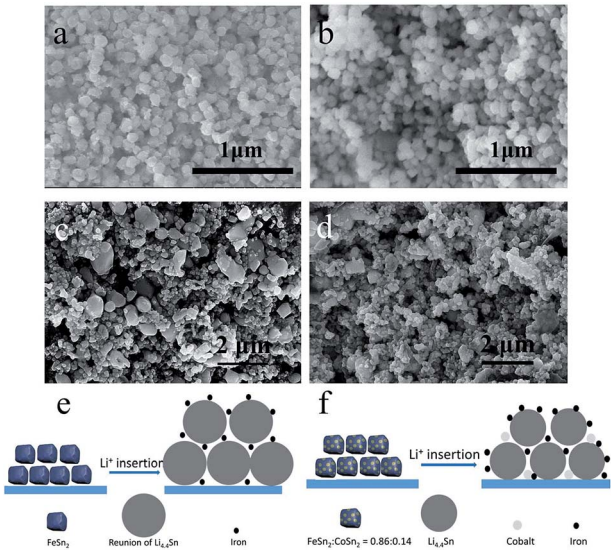

Fig. 10 (a) The SEM image of the prepared $FeSn_2$, (b) the SEM image of the prepared SnFeCo alloy, (c) the SEM image of the $FeSn_2$ electrode after 20 cycles, (d) the SEM image of the SnFeCo alloy electrode after 20 cycles, and (e and f) model of the process of lithium insertion and removal for $FeSn_2$ and SnFeCo electrodes.

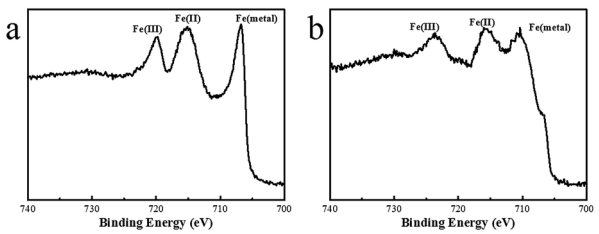

Fig. 11 The XPS spectrum of Fe 2p of (a) the $FeSn_2$ and (b) the SnFeCo placed in the air for a week.

Sn), which leads to the nonuniform particle size distribution. Note that the agglomeration can be weakened to a large extent in the multiphase because there are more phase boundaries on the surface. It is well known that the uniform nano-particles can partly accommodate the volume change and also keep the integrity of the active material and matrix, resulting in good cycle performance of the composite electrode.

From the XPS spectrum shown in Fig. 11, we can see the Fe in single-phase is more easily oxidized. This may be due to the existence of the more stable $CoSn_2$, which can reduce the exposed surface of $FeSn_2$ to some degree, resulting in higher stability. Thus, the coulombic efficiency can be improved in the multi-phase and good cycle performance can be obtained as a result.

Based on the consideration above, it is easy to visually comprehend the effect of adding cobalt to $FeSn_2$. (1) $FeSn_2$ and $CoSn_2$ can be equally distributed in the composite alloy because of their similar crystal structures, which can ensure uniform and stable chemical properties. (2) After discharging, these two alloys can be transformed to $Li_{4.4}Sn$ and the inactive pure metal M (M = Fe, Co) with equal distribution. The multiphase inactive metallic material with different densities can buffer the dimensional change during the charge/discharge process effectively. (3) These multiphase inactive metallic materials can also play an important role in keeping the integrity between the active material and the current collector, preventing pulverization at the same time. (4) The agglomeration can be weakened to a large extent in the multiphase because there are more phase boundaries on the surface. It is well known that the uniform nano-particles can partly accommodate the volume change and also keep the integrity of the active material and matrix, resulting in good cycle performance of the composite electrode. (5) The existence of the more stable $CoSn_2$ can reduce the exposed surface of $FeSn_2$ to some degree, resulting in high stability. Thus, the coulombic efficiency can be improved in the multi-phase and good cycle performance can be obtained as a result.

Conclusions

In summary, the obtained, uniform, biphasic mixture alloy composite was prepared by a facile reduction-thermal diffusion reaction. The TEM images show it is composed of Sn_2Fe and Sn_2Co. The *ab initio* simulation results indicate that the Sn_2Fe and Sn_2Co have similar crystal structures, demonstrating that the two kinds of alloys can be mixed uniformly by the thermal diffusion alloying reaction. When used as anode materials, there is a significant improvement in the cycling performance of the alloy composite. This may be due to the inactive phase M (M = Fe, Co) offering a buffer matrix to relieve the volume expansion during the charge–discharge process and also playing a role in maintaining the integrity between the particles, the active material and the current collector. Therefore, the synthesis of multicomponent alloys to obtain stable, homogeneous nanomaterial is an effective way of improving the cycling performance of tin-based anode materials.

Acknowledgements

This work was supported by the NSFC (Grant nos 21273184 and 21321062), the "973" program (Grant no. 2015CB251102) and SRFDP (20130121110002).

Notes and references

1 J. S. Chen, C. M. Li, W. W. Zhou, Q. Y. Yan, L. A. Archer and X. W. Lou, *Nanoscale*, 2009, **1**, 280–285.
2 Q. Wang, Q. Wang, D. A. Zhang, J. Sun, L. L. Xing and X. Y. Xue, *Chem.–Asian J.*, 2014, **9**, 3299–3306.
3 Q. Wang, D. A. Zhang, Q. Wang, J. Sun, L. L. Xing and X. Y. Xue, *Electrochim. Acta*, 2014, **46**, 411–418.
4 B. Liu, A. Abouimrane, D. E. Brown, X. F. Zhang, Y. Ren, Z. Z. Fang and K. Amine, *J. Mater. Chem. A*, 2013, **1**, 4376–4382.
5 L. G. Xue, X. Xia, T. Tucker, K. Fu, S. Zhang, S. L. Li and X. W. Zhang, *J. Mater. Chem. A*, 2013, **1**, 13807–13813.
6 J. Choi, S. Y. Han, J. Jin, J. Kim, J. H. Park, S. M. Lee, H. J. Kim and S. U. Son, *J. Mater. Chem. A*, 2013, **1**, 8609–8615.

7 W. Ni, J. L. Cheng, L. Y. Shi, X. D. Li, B. Wang, Q. Guan, L. Huang, G. F. Gu and H. Li, *J. Mater. Chem. A*, 2014, **2**, 19122–19130.
8 T. Brousse, R. Retoux, U. Herterich and D. M. Schleich, *J. Electrochem. Soc.*, 1998, **1**, 1–4.
9 M. Winter, I. O. Besenhard, M. E. Spahr and N. Petr, *Adv. Mater.*, 1998, **10**, 725–763.
10 J. O. Besenhard, J. Yang and M. Winter, *J. Power Sources*, 1997, **68**(1), 87–90.
11 K. D. Kepler, J. T. Vaughey and M. M. Thackray, *Electrochem. Commun.*, 1999, **1**, 111–115.
12 S. F. Fan, L. Y. Lim, Y. Y. Tay, S. S. Pramana, X. H. Rui, M. K. Samani, Q. Y. Yan, B. K. Tay, M. F. Toney and H. H. Hng, *J. Mater. Chem. A*, 2013, **1**, 14577–14585.
13 J. Yang, M. Wachtler, M. Winter and J. O. Besenhard, *Electrochem. Solid-State Lett.*, 1999, **2**(4), 161–168.
14 L. Huang, J. S. Cai, Y. He, F. S. Ke and S. G. Sun, *Electrochem. Commun.*, 2009, **11**(5), 950–953.
15 H. Guo, H. L. Zhao, X. D. Jia, J. C. He, W. H. Qiu and X. Li, *J. Power Sources*, 2007, **174**, 921–926.
16 X. L. Wang, W. Q. Han, J. J. Chen and J. Graetz, *ACS Appl. Mater. Interfaces*, 2010, **2**(5), 1548–1551.
17 X. L. Wang, M. Feygenson, H. Chen, C. H. Lin, W. Ku, J. M. Bai, M. C. Aronson, T. A. Tyson and W. Q. Han, *J. Am. Chem. Soc.*, 2011, **133**(29), 11213–11219.
18 C. Q. Zhang, J. P. Tu and X. H. Huang, *J. Alloys Compd.*, 2008, **457**, 81–85.
19 M. Chamas, P. E. Lippens, J. C. Jumas, Y. F. Yuan and S. F. Wang, *J. Power Sources*, 2011, **196**, 7011–7015.
20 G. Kresse and J. Furthmüller, *Comput. Mater. Sci.*, 1996, **6**, 15–50.
21 G. Kresse and J. Furthmüller, *Phys. Rev. B: Condens. Matter Mater. Phys.*, 1996, **54**, 11169–11186.
22 J. P. Perdew, K. Burke and M. Ernzerhof, *Phys. Rev. Lett.*, 1996, **77**, 3865–3868.
23 H. J. Monkhorst and J. D. Pack, *Phys. Rev. B: Solid State*, 1976, **13**, 5188.
24 U. G. Nwokeke, R. Alcantara, J. L. Tirado, R. Stoyanova, M. Yoncheva and E. Zhecheva, *Chem. Mater.*, 2010, **22**, 2268–2275.
25 U. G. Nwokeke, R. Alcantara, J. L. Tirado, R. Stoyanovab and E. Zhecheva, *J. Power Sources*, 2011, **196**, 6768–6771.
26 O. Mao, R. D. Dunlap and J. R. Dahn, *J. Electrochem. Soc.*, 1999, **146**, 405–413.
27 U. G. Nwokeke and R. Alcantara, *J. Alloys Compd.*, 2011, **509**, 3074–3079.
28 K. Ui, S. Kikuchi and Y. Jimba, *J. Power Sources*, 2011, **196**, 3916–3920.
29 K. Ui, S. Kikuchi, Y. N. Jimba, S. Kumagaia and S. Ito, *J. Power Sources*, 2009, **189**, 224–229.
30 T. Huang, Y. Yao and Z. Wei, *Electrochim. Acta*, 2010, **56**, 476–482.
31 R. Z. Hu, M. Q. Zeng and M. Zhu, *Electrochim. Acta*, 2009, **54**, 2843–2850.
32 N. Tamura, Y. Kato, A. Mikami, M. Kamino, S. Fujitani, M. Kamino and I. Yonezu, *J. Electrochem. Soc.*, 2006, **153A**, 1626–1632.
33 U. G. Nwokeke, F. Nacimiento, R. Alcantara and J. L. Tirado, *Electrochem. Solid-State Lett.*, 2011, **14**(10), 148–150.
34 I. A. Courtney and J. R. Dahn, *J. Electrochem. Soc.*, 1997, **144**(6), 2045–2052.

